# Facile flexible sensors based on CNT-metal oxide nanocomposites for $CO_2$ sensing

Ashok Kumar L[1], Alagappan M[2], Ria George[3], Janani K M[4]
{lak.eee@psgtech.ac.in[1], man.ece@psgtech.ac.in[2], riajoy1991@gmail.com[3], jananiaanandh@gmail.com[4]}

Department of Electrical and Electronics Engineering, PSG College of Technology Peelamedu, Coimbatore, Tamilnadu, India[1,3,4] , Department of Electronics and Communication Engineering, PSG College of Technology, Peelamedu, Coimbatore, Tamilnadu, India[2]

**Abstract.** Portable and wearable gas sensors are required to judge and warn people about the condition of the air they walk into and thus deter accidents caused by gas leakage, saving life and machinery.Synthesis and characterization of CNT / metal oxide nanocomposites with two different compositions, namely $SnO_2$ and ZnO are investigated in this paper. The nanocomposites are coated using a simple drop casting method over a flexible electrode with interdigitated geometry. The fabricated sensors are tested for $CO_2$ gas in a custom-made test set up. It was observed that $SnO_2$ and ZnO are n-type semiconductors in which resistance increased with increasing $CO_2$ concentration. The facile hydrothermal synthesis process, ease of fabrication, and room temperature operability make metal oxide Nano composites with CNT as a good candidate for $CO_2$ gas sensing.

**Keywords:** CNT/metal oxide nanocomposites, Gas sensing, Chemiresistor, Nano Sensor, Composites.

## 1 Introduction

Commercial metal oxide gas sensors available are based mainly on tin dioxide, and work based on the principle of variation in their conductivity after exposure to gas. Disadvantages of these sensors include high operation temperature, selectivity, and poor short-term stability [1,2]. The pre-heating of the sensor body before the sensing cycle for de-adhesion of the gas molecules leads to high energy consumption. The need to develop tiny, inexpensive, and flexible sensors for wearable applications has also shifted the focus in direction of nanomaterials being used for such sensing applications [3]. Controlling and altering the morphology, crystalline structure, and chemical composition of the nanomaterial during synthesis can fine-tune the gas sensing properties of the nanomaterial. [4]. In addition to the high relative surface area that increases the sensitivity, these nanomaterials also exhibit semi-conductive nature, making it possible to change the electrical conductivity based on the changes in atmospheric composition [5–7]. Several methods for depositing oxides have been created to increase the surface area of the sensor layer and hence the sensitivity [8,9]. The use of screen-printing technology for easy sensor fabrication was reported with nano metal oxides by Khmissi *et al.* and Shaban *et al.* (2016) [10,11] for gas detection. Methods such as sol-gel technique [12,13], magnetron sputtering [14], epitaxial growth [15], template synthesis [16] were used for synthesis of the nanomaterials used in the sensor. Li *et al.* (2016) [17]

ICCAP 2021, December 07-08, Chennai, India

DOI 10.4108/eai.7-12-2021.2314737

demonstrated the enhanced sensing properties due to the synergistic effects of graphene and metal oxide nanoparticles synthesized through hydrothermal technique.

Metal oxide nanostructures such as ZnO, $SnO_2$, and $Cu_2O$ have been commonly used in sensing applications with varying geometry structures like nanotubes, films, nanorods, nanotubes, nanofibers, nanowires and hollow spheres [18]. The use of CNTs as substrates in gas sensing is limited mainly by their poor selectivity which is bypassed by functionalizing the surface with metal oxides. The possibility of CNT functioning as a metal or a semiconductor based on ```the tube's diameter and chirality offers additional flexibility when matching with different metal oxides for optimal performance.

Adsorption capacity of CNTs used in sensors can be improved by purification and activation or functionalization of CNTs through methods such as oxidation to create fresh functional groups on the nanotubes surface. Functionalized nanocomposite films made of blended metal oxides, polymers mixed with metals or metal oxides, or carbon nanotubes blended with polymers, metals or metal oxides can be synthesized and implemented as active components used in gas sensors applications [19,20].

Zhang *et al.* (2012) revealed a single step technique to obtain metal oxide- decorated electrospun carbon nanofibers with core shell structure [21]. Kumar *et al.* (2006) [22] used a set chemistry path to achieve extremely hydrogen-sensitive Pt-decorated CNTs. Star *et al.* (2006) [23] decorated CNTs by selectively electroplating carbon monoxide, nitrogen dioxide, methane, hydrogen sulphide, ammonia and hydrogen with Pt, Pd, Au, Sn, Mg, Fe, Ni, and Zn [24]. In these studies, the size of the nano-clusters was a crucial factor in determining the efficiency with which the target molecule was adsorbed, and charge transfer was efficiently carried out to to influence electron transport in the nanotube [25]. Thus, the efficient electronic interaction between metal nanoparticles and the CNT promotes the detection of gases by changing these hybrid nanomaterial's electrical conductivity.

Thus, in the current paper, a comparative study of the properties of two types of nanotubular CNT-metal oxide composites - CNT- $SnO_2$ and CNT-ZnO is carried out with emphasis on their gas sensing properties.

## 2 Materials And Methods

***Synthesis of metal oxide nanocomposites***

***Precursors***

Commercially available CNTs with average diameter of 10 to 15 nm (95% purity, multiwalled, 1–5 mm length) grown by chemical vapor deposition were purchased from Merck, India. Other chemicals used include Nickel (II) chloride hexahydrate, Tin(II) chloride dihydrate , ethylene glycol, ethanol, sodium hydroxide, isopropylalcohol (IPA – 2 Proponal), potassium sodium tartrate ($C_4H_4KNaO_6$) , and sodium acetate trihydrate ($NaCH_3COO.3H_2O$), all of analytical grade and were purchased from Merck, India, and used without further purification.

***CNT Functionalization***

The following procedure was used to activate commercially available CNT by removing impurities and surface functionalization is accomplished: Initially, MWCNTs were sonicated for 1 hour in a 3:1 molar concentration combination of $HNO_3$ and $H2SO_4$. The solution was refluxed for 24 hours at 120°C in a round bottom flask and then cooled (***Fig 1***).

Diluted with distilled water, the resultant dispersion was filtered using Whatman filter paper. The oxidised MWCNTs were sonicated in deionized water and a dropwise addition of KMnO4 solution was made. The precipitate was washed and purified for residual acid extraction using a series of dilution, centrifugation, and decantation procedures until the pH was about 6. After purification, the sample was dried in an oven at 60°C overnight. Simple dispersion in distilled water was used to test the CNT's functionalization.

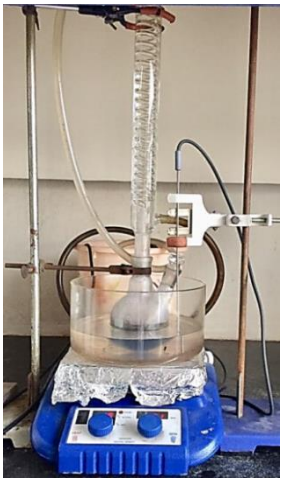

***Fig 1:*** *Photographic image of the reflux reaction setup for functionalization of CNT*

*Synthesis of CNT - $SnO_2$and CNT – ZnO nanocomposites*

The hydrothermal synthesis route for the CNT – $SnO_2$ and CNT – ZnO nanocomposites are similar. Functionalized MWCNT (0.1 g) is dispersed uniformly in a 60 ml mixed solution of ethylene glycol and water at room temperature by magnetic stirring for 1h. The tin precursor solution prepared by dissolving 0.25g of metal precursor ($SnCl_4.5H_2O$ / $ZnCl_2$) in 10 ml of ethyl alcohol is added dropwise under constant stirring for 2h. NaOH solution (0.15g of NaOH in 10 ml distilled water) is added drop wise into the CNT- metal chloride mixture under sonication. The solution is then hydrothermally treated for 12 hours in a Teflon coated stainless steel autoclave at 120°C. The autoclaved solution is cooled, centrifuged, and washed with distilled water and ethanol multiple times to separate the black coloured result. The solid product is next dried in a vacuum oven at 80°C overnight [26].

*Characterization of the metal oxide nanocomposites*

The The phase composition and crystallite size of the nanomaterials synthesized are estimated using X-Ray diffraction testing in a Philips-binary scan machine using Cu K-α (λ=1.54 Å) at 40 kV, 30 mA, over a range of 10° to 80° at a scan rate of 1°/min. The material peaks are indexed using standard JCPDF database to identify the phases present. The crystallite size of the nanomaterials was estimated from the broadened peaks using the Debye-Scherrer equation [27]

$$D = \frac{k\lambda}{B\ cos\theta}$$

where D is the grain diameter, k is the shape factor(k=0.89), $\boldsymbol{\lambda}$is the X-ray wavelength of Cu K-$\alpha$radiation (0.154 nm), $\theta$is the Bragg angle and B is the experimental full-width half maximum of the respective diffraction peak.

A UV- Vis spectroscope with an integrating sphere was used to examine the absorption spectra of the synthesized material in the ultraviolet and visible ranges (Hitachi U-3900). The

samples were dispersed in ethanol and absorption spectra was analyzed. To examine the functional groups contained in the synthesized material, the ATR-FTIR spectra was recorded on a Schimadzu Affinity IS Series Spectrophotometer. The nanocomposite powders were compacted using KBr to form pellets and absorption spectrum in the range of 4000–400 $cm^{-1}$ (2.5–25 μm) mid-infrared was recorded using a Schimadzu Affinity IS Series Spectrophotometer.

The synthesized nanomaterials were analyzed using Raman spectroscopy to investigate the interaction of carbon-based materials with other elements. Raman Spectra were recorded on a Renishaw RM1000B LRM using a 514.5 nm, Ar+ laser excitation source [28]. HR-TEM images were investigated using JEOL JEM 2100 (JEOL, Tokyo, Japan) at 300 kV accelerating voltage to understand the morphology. Qualitative analysis of the elemental composition in the synthesized material was carried out with the EDAX attachment.

*Fabrication of chemiresistor for gas chamber testing*

Commercially available PET substrate of 175μm thickness was used for screen-printing the interdigitated electrodes in the current work. Commercially available Ag-based conductive ink with nanoparticle sizes ranging from 2nm to 200 nm and metal loading ranging from 10% to 60% was used for printing the electrode in this work. The screen's surface is swept with a rubber squeegee after loading silver nanoparticle ink onto the screen, thus bringing the ink into close contact with the substrate [29]. Simultaneously, the ink flows from the screen to the substrate surface [30]. As the screen is separated from the substrate, the ink dries to produce the desired electrode.

To guarantee continuous metallic contact and excellent electrical conductivity, the screen-printed electrode was sintered at 200°C to eliminate any leftover organic stabilising agents and other non-volatile ink components [31]. The sintering process also results in an embossed effect of the printed patterns over the substrate. The sensor electrodes were then cleaned in acetone and isopropyl alcohol for 15 min and subsequently exposed to hexamethyl disilazane for 2 h to enhance the adhesion of sensing layer. Next, a micropipette deposited the prepared sonicated dispersion solutions of CNT/ metal oxide nanocomposites on the electrode structures. The deposited sensor layers were dried at 60°C for 2 h on a hot plate and then dried for 24 h in a desiccator using silica gel. ***Fig 2*** shows the schematic of the gas sensor after fabrication process and the image of interdigitated silver electrode printed on flexible PET substrate.

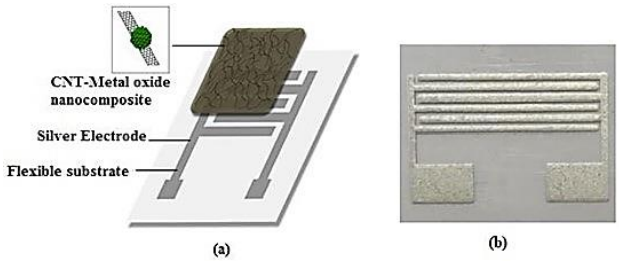


***Fig 2:*** *(a) Schematic representation of the Entire Gas Sensor (b) The Interdigitated (IDE) Electrode Fabricated on Flexible PET Substrate [32]*

The adhesion of the nanomaterials to the substrate was tested by bending the flexible sensor for 100 cycles over an angle of 90° for 100 cycles followed by visual inspection. The conductivities of the electrode patterns on PET substrates were evaluated before and after the 100 bending cycles to demonstrate the mechanical flexibility of the silver electrode models generated using screen printing. The distribution of the nanomaterials and the surface

roughness of the electrode was observed under an Atomic force Microscope in tapping mode, at a scanning velocity of 2 MHz over a region of 500 × 500 nm.

Sensor behavior in presence of $CO_2$ gas for four concentrations from 1000 ppm to 4000 ppm was tested in a custom-built gas-sensing test chamber designed using COMSOL software. The schematic and photographs of the fabricated test chambers is given in ***Fig 3***.

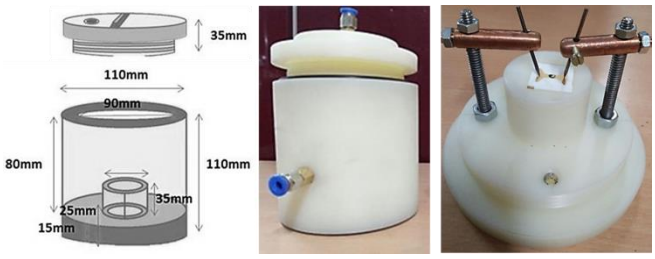


***Fig 3:*** *(a) Schematic of the gas test chamber, (b) fabricated test chamber and (c) sensor stage*

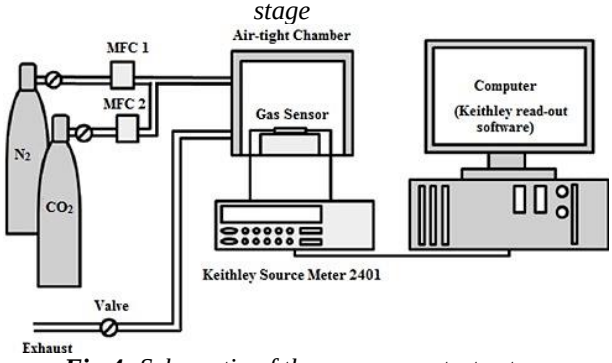


***Fig 4:*** *Schematic of the gas sensor test set up*

The gas–sensing chamber is an air-tight cylinder made of nylon, with a diameter of 110mm and height of 150mm, and a threaded top. For uniform gas distribution in the test chamber, the sensors are mounted on a stage at the bottom of the chamber, and the gas input is mounted on the top lid (***Fig 3***(c)). The entire test set up for conducting sensor-response tests is shown in ***Fig 4***.

The baseline for reference of sensor behaviour is measured by exposure to dry air over the sensor chip for 10 min. For each measurement cycle, the $CO_2$ gas stream was let in after a dry air flush for 5 min, maintained till the sensor response reached a stable level, followed by a second dry air flush of 5 min. Four concentrations of $CO_2$ between 1000 ppm and 4000 ppm were used for each sensor, and repeatability tests were performed. The studies were conducted on a fabricated device with 0.4 mm spaced, 4-leg interdigitated silver electrodes maintained at a fixed voltage of 0.01V. The readings were obtained with a Keithley Source Meter (Model No.2401) to measure the sensor's response to different $CO_2$ concentrations in the 1,500 $cm^3$volume sealed nylon chamber at room temperature. Commercial purity $N_2$ (1000 ppm) was used as carrier gas to supply varying concentrations of $CO_2$ through a mass flow controller (MFC) to the chamber, which was removed with a vacuum pump after the sensing cycle. The change in resistance values were measured across the wires bonded to the silver electrodes of the sensor positioned firmly on the stage in the bottom of the chamber. The experiments were conducted with varying gas concentration and time of exposure. The sensitivity of the sensors were determined using the equation below

$$S(\%) = \frac{(R_a - R_g)}{R_g} \times 100$$

where $R_a$ is the resistance of the sensor before injecting $CO_2$ gas and $R_g$ is the resistance obtained in the pumping half-cycle [33–35]. In addition, the gas sensor's response behavior is reflected in the response time, which is defined as the time needed to achieve 90% of the maximum change.

## 3 Results

***X-ray diffraction studies***

***Fig 5***(a) shows the X-ray diffraction data of the CNT-$SnO_2$ nanocomposite. The major diffraction peaks in the XRD data correspond to the 101, 200 and 211 $SnO_2$ cassiterite planes of tetragonal rutile structure of $SnO_2$(JCPDS card No. 41-1445) [36]. The presence of distinctive peaks of CNT (JCPDS No. 00-026-1080) indicate the formation of the composite with $SnO_2$. The mean crystalline grain size of $SnO_2$ is 4.3nm, calculated from the diffraction peak of 1 0 1 plane using Debye Scherrer equation.

***Fig 5*** (b) indicates the diffraction data of CNT-ZnO nano composites; the major peaks are identified and are found to match those of ZnO (JCPDS Card No. 01-076-0704) and MWCNT (JCPDS No. 00-026-1080) [36]. The peaks at $2\theta$= 31.32°,34.33°, 36.15°, 47.5°, 56.5°, 62.8° and 67.9° correspond to (100), (002), (101), (102), (110), (103) and (112) crystal planes in the hexagonal structure of ZnO and indicate the formation of ZnO crystallites in the composite [37]. The peaks at $2\theta$= 26° and 41° are ascribed to the MWCNT graphite framework. Between the peaks of zinc oxide, the three most intense peaks are associated with crystal plates (100), (002) and (101) as seen elsewhere. The relative intensities of the peaks in the XRD data correspond to the relative concentrations of zinc oxide precursor and MWCNT. The minor peak shifts in the XRD curves are caused by the divergence between the lattice constants of ZnO and ZnO/MWCNT grid. These changes in peaks may indicate a lattice strain between ZnO and CNT at the interface.

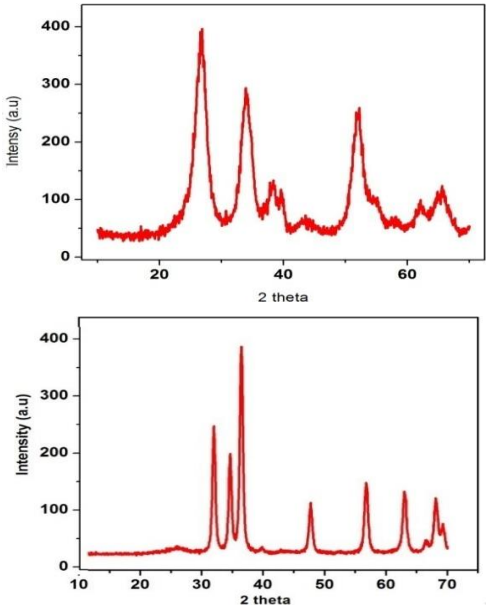


***Fig 5:*** *XRD Spectra of (a) CNT-SnO2 nanocomposite and (b) CNT-ZnO nanocomposite*

*Fourier Infrared Spectroscopy (FTIR) Results*

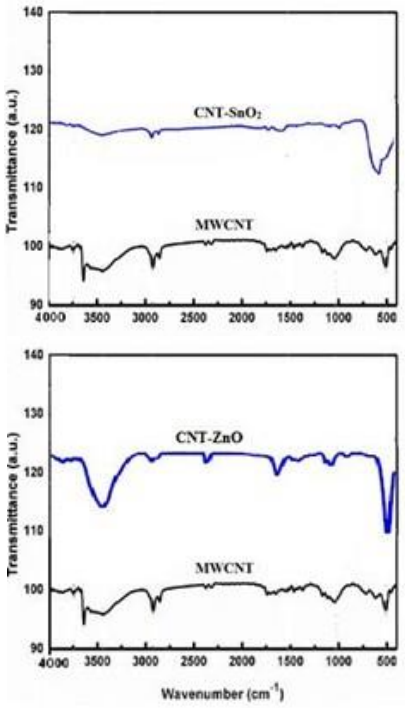


***Fig 6:*** *FTIR Spectra of Functionalized MWCNT (a) CNT-$SnO_2$ nanocomposite and (b) CNT-ZnO nanocomposite*

The stretching vibrations of the O-H, C=C, and C-O bonds caused significant vibrations at 3743 $cm^{-1}$, 1620 $cm^{-1}$ and 1050 $cm^{-1}$ in the FTIR spectra of functionalized MWCNT (***Fig 6***(a)). This indicates that functional groups like OH, COOH, and CHO might be present on the CNT's surface. Low intensity peaks of 2846 $cm^{-1}$ and 2914 $cm^{-1}$ might be vibrations of -CH and= CH, respectively, while moderate intensity bands of 1358–1460 $cm^{-1}$ could be $CH_2/CH_3$ banding vibrations. The CNT- $SnO_2$ nanocomposite (***Fig 6***(b)) showed a 588 $cm^{-1}$band characteristic of stretching vibrations from Sn-O-Sn / Sn-OH. The strong hydroxyl stretching (3443 $cm^{-1}$) and bending (1626 $cm^{-1}$) bands emerged due to the physically absorbed $H_2O$ on $SnO_2$ surface. The presence of the C-O band (1050 $cm^{-1}$) and the distinctive Sn-O band (588 $cm^{-1}$) confirms the composite structure in CNT-$SnO_2$ [28].

***UV-Vis Spectrophotometry Results***

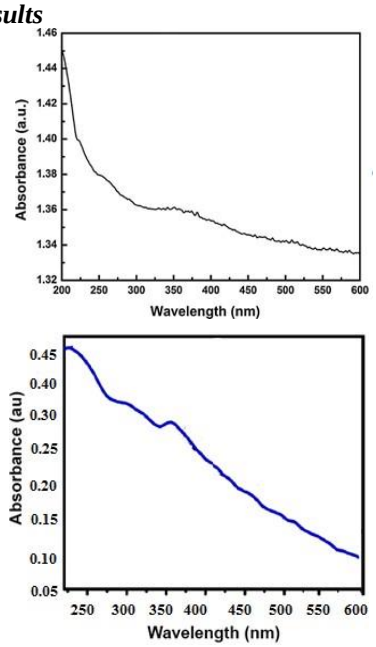


***Fig 7:*** *UV-Visible Spectra of (a) CNT-$SnO_2$ and (b) CNT-ZnO*

***Fig 7***(a) shows the absorption spectra of CNT-$SnO_2$ nanocomposite, indicating the absorption edge of CNT-$SnO_2$ located in the UV region at about 200-250 nm. The absorption threshold of pure $SnO_2$ reported in the literature is in the UV region at wavelengths between 370 and 380 nm [38]. In the presence of MWCNT, the highest absorption bands of pure $SnO_2$ shift to a lower wavelength band, supporting the formation of the nanocomposite material.

The absorption spectrum of the CNT-ZnO nanocomposite (***Fig 7***(b)) has a peak at 280 nm, compared to that of bulk ZnO is reported to be 375 nm [39]. The formation of the CNT-ZnO nanocomposite shifted the absorption edge by 0.2 eV. Dispersed MWCNTs exhibit a typical absorption band at 267nm. The solution's well-distributed MWCNTs may permit the molecular ZnO precursor to access bare surface areas for breakdown and subsequent ZnO nanocomposite formation.

***Raman Spectra of CNT-metal oxide nanocomposites***

The The functionalized MWCNT and CNT-$SnO_2$ displayed characteristic front order D and G bands at 1350.39 $cm^{-1}$ and 1605.37 $cm^{-1}$ respectively in Raman spectra, as shown in

***Fig 8***(a) and (b) respectively. This confirms the presence of carbon backbone. The G band corresponds to the tangential pyrolytic graphite stretching mode. The D-peak assigned originates from the $sp^2$ hybridized carbon defects and indicates a graphic carbon lattice distortion. The intensity ratios are therefore a measure of the magnitude of the change and the related defects on the CNT. The intensity ratio for functionalized CNT and CNT-$SnO_2$ nanocomposite material were discovered to be 0.85 and 0.92 respectively. The small rise in the intensity ratio means a reduction in the average size of $sp^2$ domains and an increase in the atomic order of the CNT surface crystallinity after being covered by $SnO_2$. In the meantime, a slight up-shift of the G-band i.e., from 1589 to 1603 $cm^{-1}$was also noted with $SnO_2$ deposition indicating an efficient transfer of charge between CNTs and $SnO_2$ [28].

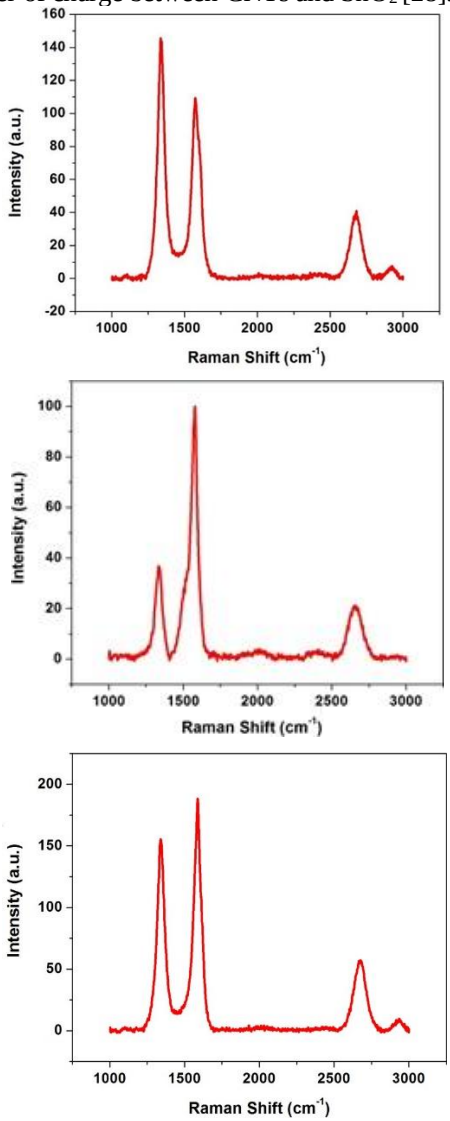


***Fig 8:*** *Raman Spectra of Functionalized (a) MWCNT, (b) CNT-$SnO_2$ nanocomposite and (c) CNT-ZnO nanocomposite*

The Raman spectra of the ZnO- MWCNT nanocomposite shown in ***Fig 8***(c) indicates first-order Raman absorptions at 1353 $cm^{-1}$for the disordered band (D) and grapheme band (G) at 1578 $cm^{-1}$ for the MWCNTs as well as second-order Raman signals at 2685 $cm^{-1}$. The increase in ratio of intensities of D to the G band ($I_D$ / $I_G$ ratio) is attributed to the disturbance in the CNT's graphical structure due to presence of oxide nanoparticles [40]. The minorpeaks between 200 and 2500 $cm^{-1}$ can be assigned to the residual isopropanol contamination ($CH_2$ bending vibration and $CH_3$ antisymmetric bending vibration) from nanomaterial dispersal solution. The in-phase vibration of carbon atoms perpendicular to the nanotube axis, called the radial breathing mode, was observed in CNTs and showed the presence of narrow CNTs (a few nanometers in diameter) [41].

***Transmission Electron Microscopy (TEM) analysis***

The TEM images of CNT-$SnO_2$ nanocomposite (***Fig 9***(a)) indicate nano particles of $SnO_2$ particles decorating the surface of multiwalled CNTs, with a rough aggregate size of 30-150 nm. Individual particles of the size of 10-15 nm are also visible. During impregnation, the particle density on the MWCNTs rises as the precursor concentration increases. The SAED patterns in ***Fig 9***(d) indicate a lattice spacing of 3.3 Å corresponding to the (110) rutile $SnO_2$ surfaces, showing the $SnO_2$'s elevated crystallinity.

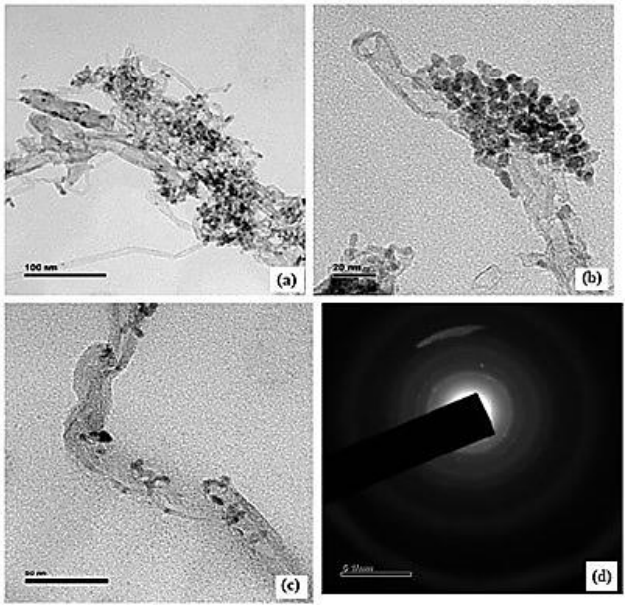


***Fig 9:*** *(a-c) HR-TEM Images and (d) SAED of CNT-$SnO_2$ nanocomposite*

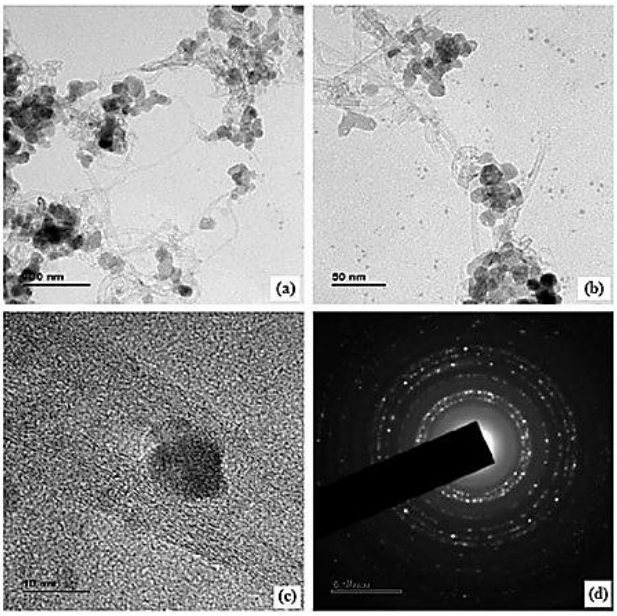


***Fig 10****: (a-c) HR-TEM Images and (d) SAED of CNT-ZnO nanocomposite*

***Fig 10***(a-c) shows the TEM images of CNT-ZnO nanocomposite. It appears that the entire surface of the multiwalled CNTs are loaded with ZnO nanospheres. The tips of the CNTs tend to be decorated with elevated particle coverage and even partial filling of the inner tube volume is noted. The average particle size is about 4.5 nm with a narrow distribution of 2–10 nm range. The image indicates that there were no unattached or isolated nanoparticles of ZnO observed in the sample, indicating the formation of the MWCNT – ZnO nanohybrid. The number density of the ZnO nanoparticles could be increasing by increasing the mass ratio of ZnO precursor to CNTs. The diffraction rings observed in the SAED pattern of CNT-ZnO in ***Fig 10***(d) suggests the polycrystalline nature of the ZnO particles and their random orientation. The crystallite lattice fringe spacing (0.33 and 0.26 nm) matches ZnO planes (100) and (101) planes.

The EDX spectral analysis of the CNT- metal oxide nanocomposites are shown in ***Fig 11***(a-b). The EDX spectra of CNT- $SnO_2$ in ***Fig 11***(a) shows the presence of Cu, O and Sn elements, with the weight percentage of Sn =15.37. ***Fig 11***(b) indicates the presence of C, O and Zn in the hybrid samples with 12.8 wt. % of Zn in the sample at the tested area.

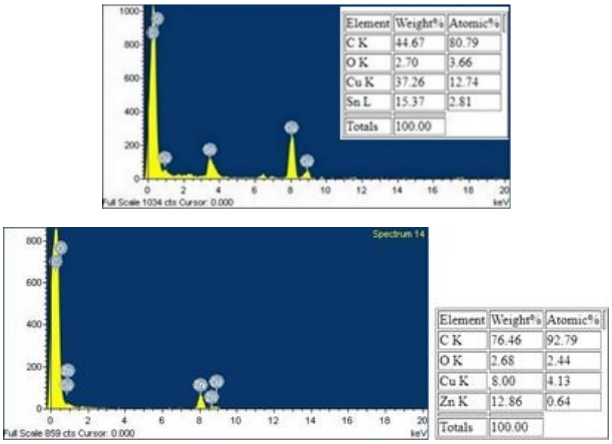


***Fig 11****: EDX Spectra of (a) CNT-$SnO_2$ and (b) CNT-ZnO*

**Characterization Of Flexible Electrode**

Visual inspection indicated that the electrode pattern adhered to the substrate even after 100 bending cycles and that pattern laid flat after the removal of the bending force. There was no significant change in the conductivity of the deposited electrode before and after 100 bending cycles. For instance, the resistance of 6-leg silver electrode with 0.4 mm gap was 23 MΩ before and after bending. In addition, the silver electrodes had no observable cracks, as shown in ***Fig 12***(a-b), indicating that silver ink screen printing can be used as a method to generate flexible patterned electrodes with adequate performance for lab based studies.

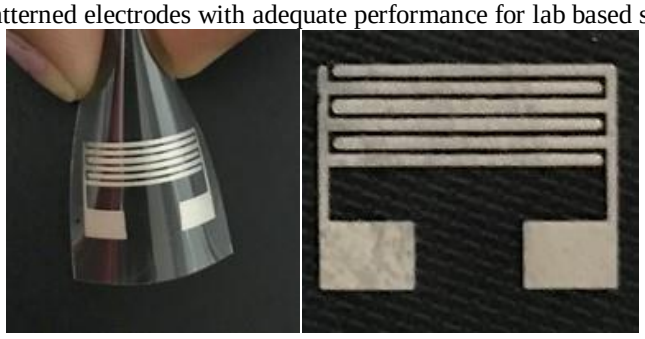

***Fig 12:*** *(a) Mechanically Flexible Electrode (b) Absence of any crack after 100 bending cycles*

**Observation of surface roughness using AFM analysis**

AFM images of the electrode coated with sensing material (***Fig 13***(a)) show particles of varying size and distribution over the chosen area of 500nm × 500nm. The electrode's surface uniformity is non-monotonically variable. The width of the deposited electrode structure and the grain size of the particles influence the surface uniformity due to the manual drop casting method employed in the fabrication. Thus, an appropriate deposition method is required for obtaining a sensing layer of uniform thickness and grain size. ***Fig 13***(b) shows the 3D image of electrode coated with sensing material.

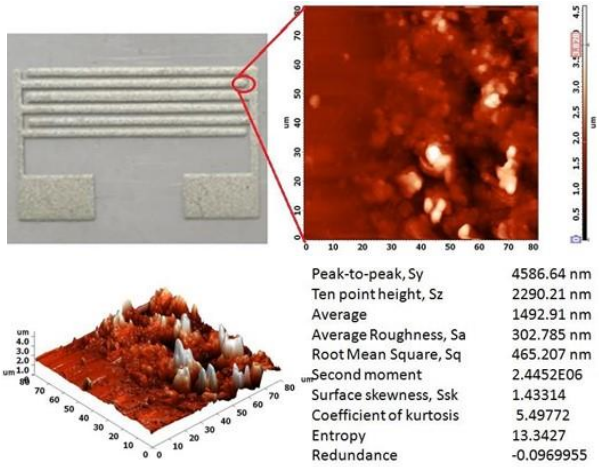


***Fig 13**: (a) 2D AFM images of the electrode (b) 3D image of electrode coated with sensing material*

**Sensor Response Towards Co2 Gas**

**Response of CNT-SnO2 based Nanosensor**

***Fig 14***(a-d) plots the responses of the CNT/$SnO_2$ sensor for 1000, 2000, 3000 and 4000 ppm respectively. The resistance of the CNT/$SnO_2$ sensor increases as the gas concentration increases with peak resistance values of 662, 653, 664 and 685 Ω for the four concentrations ranging from 1000 to 4000 ppm, respectively. The response time on the other hand decreases as the $CO_2$ concentration increases, as seen by the steeper and narrower response curves during the filling and flushing cycles.

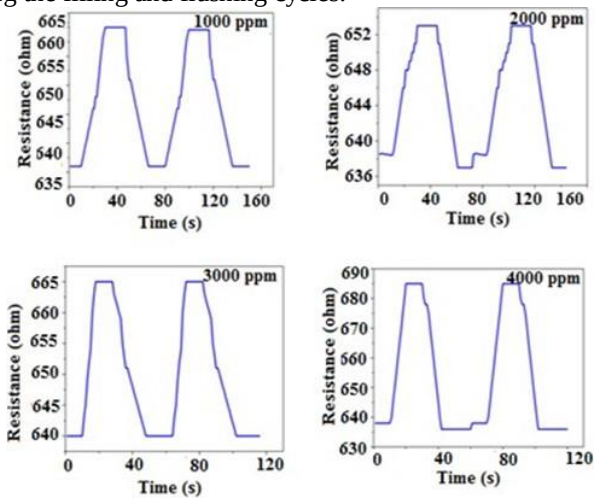


***Fig 14:** Response of CNT-$SnO_2$ Sensor towards CO2 Gas at Various Concentrations Ranging from (a)1000 ppm, (b) 2000 ppm, (c) 3000 ppm and (d) 4000 ppm*

**Response of CNT-ZnO based nanosensor**

The efficient electronic interaction between ZnO nanocrystals and the CNT makes it easier to detect gases by changing the hybrid nanostructure's electrical conductivity. ***Fig 15***(a-d) shows the sensing properties of the device towards different concentrations of $CO_2$ gas at

room temperature. The gas reaction rises with increasing CO2 concentration within the range of 1000–4000 ppm, as shown in ***Fig 15***, and the sensor responses were highly steady and repeatable [42]. The base resistance sensor made of ZnO decorated MWCNT is 471 Ω.The maximum resistance value increases from 508 to 560 Ω as the concentration of gas increases from 1000 to 4000 ppm.

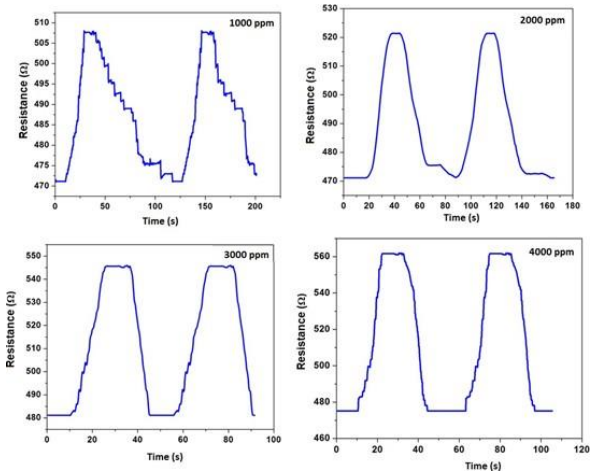


***Fig 15:*** *Response of CNT- ZnO Sensor towards $CO_2$ Gas at Various Concentrations Ranging from (a)1000 ppm, (b) 2000 ppm, (c) 3000 ppm and (d) 4000 ppm*

The response values of the different configurations and the sensitivities calculated are summarized in ***TABLE 1***.

***TABLE 1:*** *SENSOR CHARACTERISTICS*

| **Type of Sensor** | **Concentration (ppm)** | **$R_a$(Ω)** | **$R_g$(Ω)** | **Sensitivity =($R_a$-$R_g$)/$R_g$** | **$T_a$(s)** | **$T_g$(s)** | **0.9($R_a$-$R_g$)** |
|---|---|---|---|---|---|---|---|
| CNT-$SnO_2$ nanocomposite | 1000 | 638.211 | 653.310 | 2.3 | 0 | 32.02 | 13.589 |
| | 2000 | 636.745 | 660.641 | 3.6 | 0 | 30.41 | 21.501 |
| | 3000 | 640.426 | 665.021 | 3.7 | 0 | 21.29 | 22.131 |
| | 4000 | 638.511 | 685.814 | 6.8 | 0 | 18.30 | 42.572 |
| CNT-ZnO nanocomposite | 1000 | 471.021 | 495.326 | 4.9 | 0 | 38.62 | 21.879 |
| | 2000 | 471.356 | 521.668 | 9.6 | 0 | 33.06 | 45.281 |
| | 3000 | 475.219 | 545.732 | 12.9 | 0 | 25.31 | 63.461 |
| | 4000 | 475.008 | 561.063 | 15.3 | 0 | 23.66 | 77.449 |

## 4 Discussion on Sensor Characteristics

The interface properties of the MWCNT-metal oxide nanocomposite can cause a change in resistance, which can be triggered by a chemical or physical change in any part of the sensor. In the composite structure used for gas sensing, carbon nanotubes usually demonstrate p-type semiconductor characteristics, while most of the metal oxides used are n-type semiconductors (e.g. $SnO_2$ and ZnO). Hence, the junctions formed between CNTs and these metal oxides show increase in resistance in response to $CO_2$ gas. When concentration of n - type or metal oxide is high, CNTs act as an electron bridge between nanoparticles of metal oxide and show n - type behavior.

The hybrid CNT- $SnO_2$ device displays enhanced sensitivity to low-concentration gases at ambient temperature by combining high-performance CNTs with the common sensing material $SnO_2$. The sensor's base resistance is about 638 Ω at room temperature, indicating a well-conducting hybrid material. Because the work function of CNT (4.7–4.9 eV) is so near to that of $SnO_2$ (4.7 eV), the Schottky barrier between the $SnO_2$ nanocrystal and MWCNT is extremely thin, allowing electrons to flow freely between the two, with the electron transfer channel depending on the gaseous environment [43].

Target gas molecules (e.g., $CO_2$) adsorb directly to the CNT- $SnO_2$ surface, producing electron transfer and changing the hybrid nanostructure's electrical conductivity; or target gases react catalytically with oxygen adsorbents, releasing electrons back to the CNT- $SnO_2$ surface. Using electron transport between nanocrystals and carbon nanotubes, the hybrid platform enables the construction of quantum-mechanical sensing equipment.

The sensing approach is based on reactions that occur on the outermost surface of the electrode. The formation of oxygen adsorbents ($O^{2-}$or $O^{-}$) on the surface of ZnO and CNTs results in an electron-depleted surface layer as a result of electron transfer from the CNT-ZnO surface to oxygen [44]. The surface electrons are grabbed by adsorbed oxygen anions. As a result, at the MWCNT surface, a Hole Accumulation Layer (HAL) forms, producing a pseudo-insulating region at the MWCNT core and semiconductor HALs near the MWCNT surface. Holes, like p-type semiconductors, are the majority carriers, and the HAL acts as an electrical transmission channel. When $CO_2$ gas is added into the system, the density of HAL rises because $CO_2$ absorbs more valence-band electrons, causing the electrical transport channel to expand and the resistance to decrease. $CO_2$ gas molecules are engineered to adsorb on the surface of MWCNTs, creating positive holes [42].

Several factors will be ascribed to enhancing sensitivity by decorating ZnO nanoparticles. The increased surface area due to the ZnO nanocrystals enhance gas adsorption on the surface. Secondly, the spillover effect of ZnO will be identical to metal nanoparticles, facilitating the adsorption, dissociation, and migration of gas molecules. The surface defects at the hetero-interfaces of CNT / ZnO are active sites for enhanced reactivity and $CO_2$ species adsorption by altering the transfer of charge carriers across them. The activity increases with the number of p-n junctions formed between the n-ZnO and p-MWCNTs in the composite [42].

## 5 Conclusion

In this work, nanocomposites were prepared from commercially available MWCNT with two metal oxides – $SnO_2$ and ZnO with an aim to study their $CO_2$ sensing properties. The composite materials were coated on flexible substrates to prepare sensors and tested in custom

made gas chambers at room temperature. Material characterizations reveal successful formation of nanocomposites in all three cases. The chemiresistor formed by coating the synthesized materials on a silver electrode printed on a flexible PET substrate, shows good reliability and bending tolerance. The response of all the three materials to $CO_2$ gas is studied in a custom built test chamber for different concentrations from 1000 ppm to 4000 ppm and the results show good sensitivity and enhanced response as gas sensing materials due to a modulation of surface charges. Among the investigated nano materials, the metal oxides $SnO_2$ and ZnO show characteristics of n-type semiconductor. The base resistance of the CNT-$SnO_2$ junction was 638 Ω, which increased in response to $CO_2$ gas. CNT-ZnO nanocomposite showed increase in resistance from a base value of 474 Ω to a maximum of 560 Ω at 4000 ppm of $CO_2$ gas. The test results show that at maximum $CO_2$ gas concentration of 4000 ppm, the measured sensitivities were around 6.8% and 15.3% for CNT-$SnO_2$ and CNT-ZnO nanocomposites, respectively.

## Acknowledgment

The authors acknowledge University Grants Commission for funding this work. This paper is the part of the work carried out under the project Design & Development of Wireless Embedded Microcontroller Based Portable Nano Scale Toxic Gas Sensor System funded under UGC MRP Scheme.

## References

[1] N. Barsan, D. Koziej, and U. Weimar, Sensors Actuators, B Chem. 121, 18 (2007).
[2] X. Liu, S. Cheng, H. Liu, S. Hu, D. Zhang, and H. Ning, Sensors (Switzerland) 12, 9635 (2012).
[3] W. A. D. M. Jayathilaka, K. Qi, Y. Qin, A. Chinnappan, W. Serrano-García, C. Baskar, H. Wang, J. He, S. Cui, S. W. Thomas, and S. Ramakrishna, Adv. Mater. 31, 1 (2019).
[4] P. Grammatikopoulos, S. Steinhauer, J. Vernieres, V. Singh, and M. Sowwan, Http://Dx.Doi.Org/10.1080/23746149.2016.1142829 1, 81 (2016).
[5] I. Khan, K. Saeed, and I. Khan, Arab. J. Chem. 12, 908 (2019).
[6] M. S. Chavali and M. P. Nikolova, SN Appl. Sci. 2019 16 1, 1 (2019).
[7] Nadeem Baig, Irshad Kammakakam, and Wail Falath, Mater. Adv. 2, 1821 (2021).
[8] C. Wang, L. Yin, L. Zhang, D. Xiang, and R. Gao, Sensors (Basel). 10, 2088 (2010).
[9] P. Patial and M. Deshwal, Trans. Electr. Electron. Mater. 2021 1 (2021).
[10] H. Khmissi, A. M. El Sayed, and M. Shaban, J. Mater. Sci. 2016 5112 51, 5924 (2016).
[11] M. Shaban, M. Mustafa, and A. M. El Sayed, Mater. Sci. Semicond. Process. 56, 329 (2016).
[12] S. K. Shukla, G. K. Parashar, A. P. Mishra, P. Misra, B. C. Yadav, R. K. Shukla, L. M. Bali, and G. . Dubey, Sensors Actuators B Chem. 98, 5 (2004).
[13] M. Aziz, S. Saber Abbas, and W. R. Wan Baharom, Mater. Lett. 91, 31 (2013).
[14] J. Liang, Q. Liu, T. Li, Y. Luo, S. Lu, X. Shi, F. Zhang, A. M. Asiri, and X. Sun, Green Chem. 23, 2834 (2021).
[15] D. Shahrjerdi, B. Hekmatshoar, S. W. Bedell, M. Hopstaken, and D. K. Sadana, J. Electron. Mater. 41, 494 (2012).
[16] H. Xie, C. Sheng, X. Chen, X. Wang, Z. Li, and J. Zhou, Sensors Actuators, B Chem. 168, 34 (2012).
[17] X. Li, Y. Zhao, X. Wang, J. Wang, A. M. Gaskov, and S. A. Akbar, Sensors Actuators, B Chem. 230, 330 (2016).
[18] D. Zappa, V. Galstyan, N. Kaur, H. M. M. Munasinghe Arachchige, O. Sisman, and E. Comini, Anal. Chim. Acta 1039, 1 (2018).

[19] F. S. A. Khan, N. M. Mubarak, M. Khalid, M. M. Khan, Y. H. Tan, R. Walvekar, E. C. Abdullah, R. R. Karri, and M. E. Rahman, Https://Doi.Org/10.1080/10408436.2021.1935713 1 (2021).
[20] G. Korotcenkov, Sensors Actuators B Chem. 107, 209 (2005).
[21] L. Zhang, X. Wang, Y. Zhao, Z. Zhu, and H. Fong, Mater. Lett. 68, 133 (2012).
[22] M. K. Kumar and S. Ramaprabhu., J. Phys. Chem. B 110, 11291 (2006).
[23] * Alexander Star, Vikram Joshi, Sergei Skarupo, and David Thomas, and J.-C. P. Gabriel†, J. Phys. Chem. B 110, 21014 (2006).
[24] E. Llobet, Sensors Actuators, B Chem. 179, 32 (2013).
[25] R. Leghrib, A. Felten, F. Demoisson, F. Reniers, J. J. Pireaux, and E. Llobet, Carbon N. Y. 48, 3477 (2010).
[26] C. Deng, Q. Huang, X. Zhu, Q. Hu, W. Su, J. Qian, L. Dong, B. Li, M. Fan, and C. Liang, Appl. Surf. Sci. 389, 1033 (2016).
[27] M. Ahmaruzzaman, D. Mohanta, and A. Nath, Sci. Rep. 9, (2019).
[28] S. Xu, Y. Dall'Agnese, G. Wei, C. Zhang, Y. Gogotsi, and W. Han, Nano Energy 50, 479 (2018).
[29] S. Wang, N. Liu, C. Yang, W. Liu, J. Su, L. Li, C. Yang, and Y. Gao, RSC Adv. 5, 85799 (2015).
[30] A. Kamyshny and S. Magdassi, Small 10, 3515 (2014).
[31] R. George, L. A. Kumar, M. Alagappan, E. Engineering, E. Engineering, A. Professsor, and E. Engineering, 14, 213 (2019).
[32] P. Viswanathan, A. K. Patel, J. Pawar, A. Patwardhan, and R. Henry, Https://Doi.Org/10.1080/03772063.2018.1502625 66, 460 (2018).
[33] M. Y. Rezk, J. Sharma, and M. R. Gartia, Nanomater. 2020, Vol. 10, Page 2251 10, 2251 (2020).
[34] K.-M. Kim, H.-M. Jeong, H.-R. Kim, K.-I. Choi, H.-J. Kim, and J.-H. Lee, Sensors (Basel). 12, 8013 (2012).
[35] M. Achehboune, M. Khenfouch, I. Boukhoubza, B. Mothudi, I. Zorkani, and A. Jorio, J. Phys. Conf. Ser. 1292, (2019).
[36] J. Mayandi, M. Marikkannan, V. Ragavendran, and P. Jayabal, J. Nanosci. Nanotechnol. 2, 707 (2014).
[37] J. Khanderi, R. C. Hoffmann, A. Gurlo, and J. J. Schneider, J. Mater. Chem. 19, 5039 (2009).
[38] I. Sharafeldin, S. Garcia-Rios, N. Ahmed, M. Alvarado, X. Vilanova, and N. K. Allam, J. Environ. Chem. Eng. 9, 104534 (2021).
[39] J. Kennedy, F. Fang, J. Futter, J. Leveneur, P. P. Murmu, G. N. Panin, T. W. Kang, and E. Manikandan, Diam. Relat. Mater. 71, 79 (2017).
[40] Y. J. Kwon, A. Mirzaei, S. Y. Kang, M. S. Choi, J. H. Bang, S. S. Kim, H. W. Kim, Y. J. Kwon, A. Mirzaei, S. Y. Kang, M. S. Choi, J. H. Bang, S. S. Kim, and H. W. Kim, ApSS 413, 242 (2017).
[41] G. Lu, L. E. Ocola, and J. Chen, Adv. Mater. 21, 2487 (2009).
[42] S. Hosseini Largani and M. Akbarzadeh Pasha, Int. Nano Lett. 2016 71 7, 25 (2016).